Research article

Ray Jia Hong Ng, Ravikumar Venkat Krishnan, Hao Wang and Joel K.W. Yang*

# Darkfield colors from multi-periodic arrays of gap plasmon resonators

https://doi.org/10.1515/nanoph-2019-0414
Received October 8, 2019; revised December 2, 2019; accepted December 3, 2019

**Abstract:** We present results on colors of metal disk arrays viewed under a darkfield microscope and show that the darkfield colors can be manipulated independently of the brightfield colors. We investigate the appearance of colors as disks are clustered to form a new array with double the pitch and a basis of four disks. These structures of aluminum disks on aluminum oxide on aluminum have resonances in the visible spectrum, so by arranging them in small tight clusters, a coupled plasmon resonant mode is produced at shorter wavelengths. This feature causes a reflectance minimum and leads to an increase in the gamut of darkfield colors produced. These colors are tuned by changing the size of the disk and the inter-disk gap within the clusters. Interestingly, the intensities of the reflectance peaks also demonstrate good agreement with the Fourier series coefficients for square waves. Polarization-tunable colors are also demonstrated by designing rectangular arrays that have dissimilar periods along the two orthogonal axes of the array, and a four-level security tag is fabricated that encodes images for viewing under brightfield, darkfield (both $x$ and $y$ polarization), and infrared illumination.

**Keywords:** optics; color; surface plasmons; darkfield microscopy.

***Corresponding author: Joel K.W. Yang,** Singapore University of Technology and Design, Engineering Product Development Pillar, 8 Somapah Road, Singapore 487372, Singapore; and Institute of Materials Research and Engineering, A*STAR (Agency for Science, Technology, and Research), 2 Fusionopolis Way, #08-03 Innovis, Singapore 138634, Singapore, e-mail: joel_yang@sutd.edu.sg
**Ray Jia Hong Ng, Ravikumar Venkat Krishnan and Hao Wang:** Singapore University of Technology and Design, Engineering Product Development Pillar, Singapore 487372, Singapore. https://orcid.org/0000-0003-2540-2922 (R.J.H. Ng). https://orcid.org/0000-0001-5388-6691 (H. Wang)

## 1 Introduction

Plasmonic resonators have been widely studied for generating colors, as they exhibit size- and material-based tunable resonances [1–3]. Thus, they are a high-resolution alternative to traditional dyes and pigments for printing [4–6]. An interesting application of plasmonic colors is in security prints, as the resonator structures can be used to generate multiple images in one print, by selecting the polarization of illumination or collected light [7, 8], incorporating upconversion or fluorescent particles for responsivity beyond visible light [9, 10], laser-printing three-dimensional plasmonic nanovolcanoes [11], and using metal-insulator-metal (MIM) structures that can support multiple resonance modes from ultraviolet to infrared [12]. We recently demonstrated micro tags consisting of MIM structures made of aluminum with a sub-10 nm insulating layer. These structures support gap plasmons from ultraviolet to infrared wavelengths and are capable of encoding multiple sets of information [13].

Though plasmonic colors can be viewing-angle independent, increasing the periodicity of the arrays beyond ~250 nm would result in diffraction with illumination and/or viewing at glancing angles [14, 15]. This sparser arrangement allows for the structures to be observable under darkfield illumination, as they would diffract certain wavelengths of light that satisfy the grating condition. Darkfield colors have been previously reported for individual plasmonic nano-resonators [16–19], while vibrant darkfield colors have been demonstrated by arrays of such resonators [20, 21]. However, a clear understanding of the intensity of the diffracted light from these resonator arrays and its dependence on the array geometry is currently lacking. Furthermore, decreasing the density of the resonators would result in changes in their brightfield color [22]. Hence, a systematic analysis of structures that exhibit unchanging brightfield colors while varying darkfield colors due to small variations in the positioning of disks in the array is here needed. A few previous studies had also discussed the optical response of fixed clusters of resonators, but the focus was on simple metallic nanostructures rather than on gap plasmonic resonators [23–25].

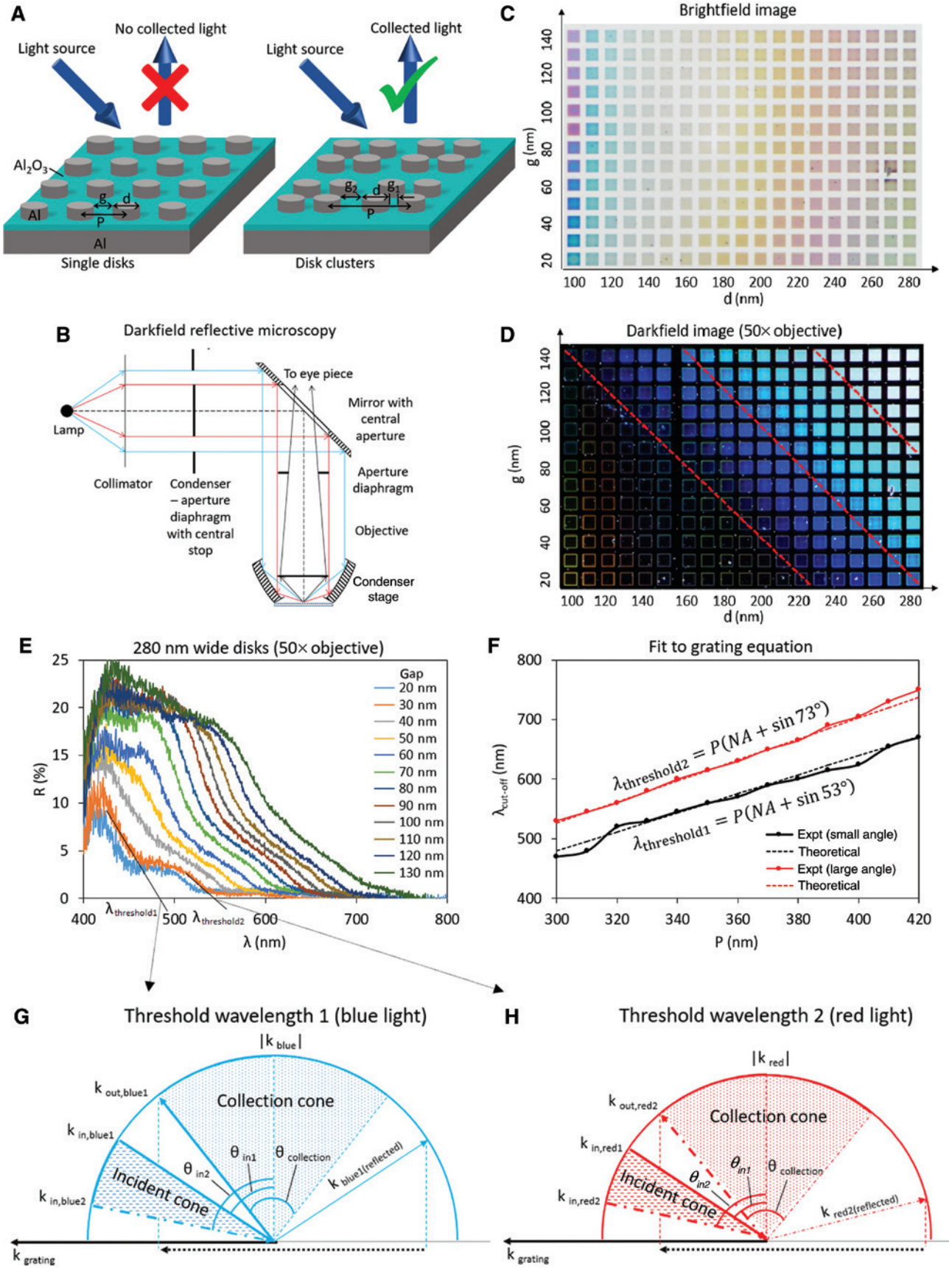
A
No collected light
Light source
Collected light
Light source
$Al_2O_3$
Al
g
d
P
Al
Single disks
$g_2$
d
$g_1$
P
Disk clusters
B
Darkfield reflective microscopy
To eye piece
Mirror with central aperture
Lamp
Aperture diaphragm
Collimator
Condenser – aperture diaphragm with central stop
Objective
Condenser stage
C
Brightfield image
g (nm)
d (nm)
D
Darkfield image (50× objective)
g (nm)
d (nm)
E
280 nm wide disks (50× objective)
R (%)
λ (nm)
Gap
20 nm
30 nm
40 nm
50 nm
60 nm
70 nm
80 nm
90 nm
100 nm
110 nm
120 nm
130 nm
$\lambda_{threshold1}$
$\lambda_{threshold2}$
F
Fit to grating equation
$\lambda_{cut-off}$ (nm)
P (nm)
$\lambda_{threshold2} = P(NA + \sin 73°)$
$\lambda_{threshold1} = P(NA + \sin 53°)$
Expt (small angle)
Theoretical
Expt (large angle)
Theoretical
G
Threshold wavelength 1 (blue light)
$|k_{blue}|$
$k_{out,blue1}$
Collection cone
$k_{in,blue1}$
$\theta_{in1}$
$\theta_{collection}$
$\theta_{in2}$
$k_{blue1(reflected)}$
Incident cone
$k_{in,blue2}$
$k_{grating}$
H
Threshold wavelength 2 (red light)
$|k_{red}|$
$k_{out,red2}$
Collection cone
$k_{in,red1}$
$\theta_{in1}$
$\theta_{collection}$
$\theta_{in2}$
Incident cone
$k_{in,red2}$
$k_{red2(reflected)}$
$k_{grating}$

**Figure 1:** Darkfield colors from arrays of single Al nanodisk gap plasmon resonators.
(A) 3D schematic of an array of Al disks on $Al_2O_3$ on Al, forming gap plasmon resonators. The disks have diameter *d*, inter-disk gap *g*, and period *P*. (B) Light paths in darkfield microscopy, where the central part of the light from the source is blocked by the central stop. Light is sent onto the sample as a hollow cone. The paths followed by the two threshold wavelengths are marked blue and red, respectively. (C) Optical brightfield micrograph taken using a Nikon 20×/0.45 NA objective. (D) Optical darkfield micrograph taken using a Nikon 50×/0.8 NA objective. Each square in the micrographs is 10 μm by 10 μm in size. The disk diameter range is 60 nm to 280 nm, while the inter-disk gap range is 30 nm to 140 nm. Saturated blue colors appear when the period increases above 250 nm. (E) Darkfield spectra for 280 nm wide disks and inter-disk gaps between 20 nm and 130 nm. The threshold wavelengths for the array with a gap of 30 nm are shown. (F) Fits of the experimental threshold wavelengths to the values obtained from the diffraction grating equation. (G) Wave vector diagram for blue light at the threshold wavelength for complete collection of first-order diffracted light. Light is incident onto the grating in a wedge of angles, where $\theta_{in1}$ and $\theta_{in2}$ correspond to the minimum and maximum polar angles, respectively. All the output angles of the diffracted light from the grating lie within the collection cone of the objective. (H) Wave vector diagram for red light. The output angle of the diffracted light lies just outside the collection cone, so no diffracted light is collected.

In this paper, we use arrays of aluminum disk gap plasmon resonators to produce colors viewable in darkfield illumination. In darkfield imaging, the colors of arrays of single disks are primarily controlled by the array periods, while those for arrays of disk clusters are affected by both the period and the inter-disk gap within the clusters. Polarization-tunable darkfield colors are also achieved by varying the periods of the array in the *x* and *y* axes. This effect gives the possibility of hiding two darkfield images in a featureless brightfield color print and of making an optical micro-print that can encode up to four images using only circular disk gap plasmon resonators that have different sizes and periods. The covertness of the darkfield images has potential applications for currency anti-counterfeiting, document and artwork authentication, and information encryption.

# 2 Materials and methods

## 2.1 Structure of resonator

The structure of the plasmonic pixel consists of a square array of Al disks lying on an $Al_2O_3$-Al-bulk silicon substrate, as shown in Figure 1A. The height of the disks is 44 nm, while the diameter *d* is between 100 nm and 280 nm. The thickness of the $Al_2O_3$ layer is 7 nm between the disk and the Al film and 4 nm elsewhere, while the thickness of the underlying Al layer is 100 nm. A ~3 nm thick layer of native $Al_2O_3$ is present all around the top and sides of the disks due to oxidation by air [12].

The fabrication process has been reported previously by Ng et al. [13]. Briefly, the first step is the deposition of a 100 nm layer of Al onto a silicon wafer using an electron-beam evaporator. After waiting for 1 day, the Al oxidizes and forms a 3 nm thick layer of $Al_2O_3$. The second step is the spin-coating of poly(methyl methacrylate) resist onto the wafer and patterning using electron beam lithography (EBL). The next step is the evaporation of 44 nm of Al, and the final step is lift-off of the resist in N-methyl-2-pyrrolidone solvent.

## 2.2 Darkfield microscopy

In optical microscopy, there are two main modes of illuminating a sample – brightfield and darkfield. In brightfield microscopy, light from the source is collected and sent onto the sample in a solid cone that is perpendicular to the sample, and the reflected or transmitted light is collected by lenses and directed to the observer. The image contrast and colors are a consequence of the absorption of certain wavelengths of light by the sample. However, in darkfield microscopy, the central circular region of the light from the source is blocked, so that a hollow cone of light is sent onto the sample instead. The darkfield image and its colors are formed by scattered and diffracted light that is directed to the central acceptance cone of the microscope objective (Figure 1B). Scattering of light can be performed by a single particle, whereas diffraction requires a large periodic array of particles.

The incident and collected light in a microscope can be characterized in terms of their wave vectors and angles. The equation $\theta = \sin^{-1}$ NA is used to calculate the half-acceptance angle of the acceptance cone, where NA is the numerical aperture of the objective. For a darkfield microscope, the wave vector of the incident light makes an angle that is bounded by upper and lower limits, which are associated with the outer and inner circumferences of the ring of light, respectively. The lower limit is necessarily greater than the half-acceptance angle. The incident wave vector thus has both large in-plane and out-of-plane components, and in order for the light to be scattered and diffracted off

the sample to be collected by the objective, an in-plane wave vector must be added in the opposite direction to the incident wave vector to force the resultant wave vector to fall within the acceptance cone of the objective. In practice, many modern optical microscopes have integrated components for performing brightfield and darkfield measurements, so the microscope body has a retractable central stop piece, and special microscope objectives can be used for both brightfield and darkfield imaging.

## 2.3 Diffraction by gratings

The wave vector of a one-dimensional simple grating, $\boldsymbol{k}_{\mathbf{grating}}$, has a magnitude given by $2\pi/P$, where $P$ is the period, and a direction that is perpendicular to the axis of the grating and in-plane with the grating. For any wavelength of light $\lambda$ the input light from a microscope has a wave vector in air, $\boldsymbol{k}_{\mathbf{in}}$, whose magnitude is given by $2\pi/\lambda$, while the direction is determined by the light path through the optical components. Thus, the shortest blue wavelengths of light (~400 nm) have the largest wave vectors, while the longest red wavelengths (~700 nm) have the smallest wave vectors. When light is reflected by a perfect reflector, the wave vector of the reflected light retains its original magnitude, but the vertical or $z$-component of the vector reverses its sign.

Wave vector diagrams can be used to explain the diffraction of the input light, as shown in Figure 1G and H, for the case of a one-dimensional grating. The grating wave vector, incident and output wave vectors, and incident and collection cones are as indicated. (The right half of the incident cone is omitted for clarity.) We consider the case where the grating vector $\boldsymbol{k}_{\mathbf{grating}}$ has a larger magnitude than the wave vectors of the input light, as the period of the disk array is smaller than the wavelength of violet light, which is 380 nm. The incident cone for a 50×/0.8 NA objective has incident angles between ~53° and 73°. The input and output wave vectors lie on a circle because of conservation of energy. To find the direction of the output wave vector for a particular input angle, in-plane phase matching along the $x$-direction is used (the magnitudes of the vectors $\boldsymbol{k}_{\mathbf{grating}}$, $\boldsymbol{k}_{\mathbf{in},x}$, and $\boldsymbol{k}_{\mathbf{in},y}$ are not in bold):

$$k_{\mathrm{out},x} = k_{\mathrm{in},x} - m k_{\mathrm{grating}}, \tag{1}$$

$$\frac{2\pi}{\lambda}\sin\theta_{\mathrm{out}} = \frac{2\pi}{\lambda}\sin\theta_{\mathrm{in}} - m\left(\frac{2\pi}{P}\right), \tag{2}$$

$$\sin\theta_{\mathrm{out}} = \sin\theta_{in} - m\left(\frac{\lambda}{P}\right). \tag{3}$$

The diffraction order, $m$, is taken as positive, as negative values would give a diffraction angle that lies outside the collection cone. $\theta_{\mathrm{in}}$ and $\theta_{\mathrm{out}}$ are measured with respect to the normal to the surface and are limited to the upper half-plane ($z>0$). By definition, if the output wave vector lies in the same quadrant as the input vector, then $\theta_{\mathrm{out}}$ is negative, whereas $\theta_{\mathrm{out}}$ is positive if the output and input wave vectors lie in different quadrants. From Eq. (3), $\theta_{\mathrm{out}}$ is negative when the magnitude of $\boldsymbol{k}_{\mathbf{in},x}$ is smaller than that of $m\,\boldsymbol{k}_{\mathbf{grating}}$. With small periodicities, no light is collected as $\boldsymbol{k}_{\mathbf{grating}}$ is too large. However, with increasing periodicity $\boldsymbol{k}_{\mathbf{grating}}$ decreases, and we start to observe some light.

In Figure 1G we consider the specific condition where the input light is blue and has an incident angle equal to the smallest angle of the incident light cone ($\theta_{\mathrm{in1}}$). This illumination with wave vector $\boldsymbol{k}_{\mathbf{in,blue1}}$ is diffracted and deflected in the opposite direction such that the output light $\boldsymbol{k}_{\mathbf{out,blue1}}$ just fits into the collection cone ($|\theta_{\mathrm{out}}| < \theta_{\mathrm{collection}}/2$). For larger incident angles, e.g. for $\boldsymbol{k}_{\mathbf{in,blue2}}$, the input $x$-component increases, so the output light $\boldsymbol{k}_{\mathbf{out,blue2}}$ has a smaller $x$-component and easily fits into the collection cone. Thus, all the first-order diffracted blue light, regardless of incident angle, is collected by the objective. The threshold (maximum) wavelength at a particular incident angle for which light will be first-order diffracted into the collection cone of the objective occurs when $\theta_{\mathrm{out}}$ is equal to $-\sin^{-1}$ NA, or $\sin\theta_{\mathrm{out}} = -\mathrm{NA}$. $\theta_{\mathrm{out}}$ has a negative sign as it lies in the same quadrant as $\theta_{\mathrm{in}}$. Thus, the following equations apply, where $\theta_{\mathrm{in1}} < \theta_{\mathrm{in2}}$ and $\lambda_{\mathrm{threshold1}} < \lambda_{\mathrm{threshold2}}$:

$$m\lambda_{\mathrm{threshold1}} = P(NA + \sin\theta_{\mathrm{in1}}), \tag{4}$$

$$m\lambda_{\mathrm{threshold2}} = P(NA + \sin\theta_{\mathrm{in2}}). \tag{5}$$

Figure 1H shows the wave vector diagram for red light. Since red light has a longer wavelength than blue light, its wave vector is shorter and the $x$-component of the diffracted light is larger, producing a larger output angle that falls outside of the collection cone, e.g. for $\boldsymbol{k}_{\mathbf{in,red1}}$. This condition applies for all the incident angles of red light smaller than $\theta_{\mathrm{in2}}$, which is the largest angle of the incident light cone. Therefore, in contrast to the case for blue light, almost no red light is collected by the objective. The resultant spectrum collected by the objective will mostly consist of short blue wavelengths of light, and thus the image will appear blue.

Since the disk arrays are two-dimensional, the diffraction grating vector is not fixed along one axis and can point in various directions. In fact, there are two grating vectors, $\boldsymbol{k}_{\mathbf{grating},x}$ and $\boldsymbol{k}_{\mathbf{grating},y}$, and two boundary conditions to be satisfied. For the disk arrays in this section, the

$x$-period $P_x$ and $y$-period $P_y$ are the same ($P_x = P_y = P$), so the magnitudes of $\boldsymbol{k}_{\mathbf{grating},x}$ and $\boldsymbol{k}_{\mathbf{grating},y}$ are the same. In general,

$$k_{\mathrm{out},x} = k_{\mathrm{in},x} - mk_{\mathrm{grating},x} = k_{\mathrm{in},x} - m\left(\frac{2\pi}{P_x}\right) \tag{6}$$

$$k_{\mathrm{out},y} = k_{\mathrm{in},y} - nk_{\mathrm{grating},y} = k_{\mathrm{in},y} - n\left(\frac{2\pi}{P_y}\right) \tag{7}$$

$$k_{\mathrm{out},z} = \sqrt{{k_{\mathrm{in}}}^2 - {k_{\mathrm{out},x}}^2 - {k_{\mathrm{out},y}}^2} = \sqrt{{k_{\mathrm{in}}}^2 - \left(k_{\mathrm{in},x} - m\left(\frac{2\pi}{P_x}\right)\right)^2 - \left(k_{\mathrm{in},y} - n\left(\frac{2\pi}{P_y}\right)\right)^2} \tag{8}$$

When the array period is small, only the first-order diffracted light in either the $x$- or $y$-direction can be collected, so the disk array can be analyzed in terms of a one-dimensional (1D) grating.

Brightfield and darkfield images of the Al nanodisk arrays are taken using a Nikon Eclipse LV100ND microscope and shown in Figure 1C and D. A 50×/0.8 NA objective is used, which corresponds to a half-acceptance angle of 53°. In Figure 1D, saturated blue and cyan colors are observed for arrays with large periods greater than 250 nm. These colors form bands of similar color along the diagonal, as the array periods are constant along each diagonal line from the upper left to the lower right. These colors are caused by diffraction, as explained in the previous section. For periods around 250 nm, only short wavelengths of light are diffracted by the array and collected by the objective, so the arrays appear blue. When the period increases, longer green wavelengths are also collected, so the arrays appear cyan.

For arrays with smaller disk diameters (<240 nm), the central part of the array appears black but the square borders are colorful due to enhanced plasmon scattering by the individual disks, spanning blue, green, yellow, orange, and red. These colors are size-dependent and remain the same throughout each column of arrays and had been demonstrated previously using gold nanoparticles separated from a gold film by a sub-nanometer spacer [26].

The reflectance spectra for arrays of 280 nm wide disks were measured with a CRAIC 508 PV spectrophotometer and show a clear peak-and-side-lobe profile (Figure 1E). The inter-disk gap $g$ is varied from 20 nm to 130 nm; thus, the periods $P$ are 300 nm to 410 nm. The peaks in the spectra occur around 400 to 450 nm and increase in amplitude when the period increases. The reflectance gradually decreases to nearly 0 at a characteristic threshold wavelength. This threshold wavelength is the maximum wavelength at which the diffracted light from the array falls into the collection cone of the objective. Since the incident light cone has a spread of polar angles, there are two threshold wavelengths, $\lambda_{\mathrm{threshold1}}$ and $\lambda_{\mathrm{threshold2}}$, corresponding to the minimum and maximum polar angles, respectively. Both threshold wavelengths redshift when the inter-disk gap increases. The threshold wavelengths are also compared to the theoretical prediction in Figure 1F and show good agreement. Here the theoretical relationship between the threshold wavelength and the array period is obtained from the diffraction grating equation, where the diffraction order $m$ is +1:

$$\lambda_{\mathrm{threshold}} = P(NA + \sin\theta_{\mathrm{in}}). \tag{9}$$

# 3 Results

## 3.1 Polarization-dependent darkfield images

Polarization-dependent brightfield colors have been previously demonstrated using asymmetric plasmonic structures, e.g. rods, ellipses, and crosses, so that the plasmon resonances along one principal axis have a different frequency from those along the orthogonal axis [7, 8, 27–29]. However, with darkfield colors, instead of changing the shape of the resonator, polarization dependence can be introduced by having different array periods along the $x$- and $y$-axes, which causes the grating vectors to have different magnitudes. As the resonators themselves are circular, the brightfield colors will not have polarization dependence, as the plasmon resonance frequencies are determined by the resonator geometry and less influenced by rearrangement of the disks.

One type of multi-periodic disk array was fabricated – a rectangular array of 200 nm wide disks with dissimilar $x$- and $y$-periods. The arrays are observed using a darkfield microscope with a linear polarizer placed in the light path between the source and the sample. When the direction of the polarizer axis is 0°, in other words parallel to the $x$-axis, the electric field of the wave that has passed through the polarizer points along the $x$-axis. Now, if the azimuthal angle $\phi$ is 0° or 180°, the incident electromagnetic wave

**Table 1:** Dependence of polarization of incident light on azimuthal angle and orientation of linear polarizer.

| Azimuth $\phi$ | $x$-polarizer | $y$-polarizer |
|---|---|---|
| 0°, 180° (east, west) | $p$-polarization | $s$-polarization |
| 90°, 270° (north, south) | $s$-polarization | $p$-polarization |

is *p*-polarized relative to the sample. When the polarizer is rotated by 90°, the electromagnetic wave becomes *s*-polarized for an azimuthal angle of 0° or 180°. The above results about the polarization properties of the incident light are summarized in Table 1. The diffraction efficiency of the disk grating array is higher for *p*-polarized incident light than for *s*-polarized light, since the *p*-polarized light couples better to the surface plasmons, as will be discussed below via simulation results.

The schematic for the disk array is shown in Figure 2A, where the *x*-period and *y*-period are indicated by $P_x$ and $P_y$, respectively. The disk diameter was 200 nm, while both $P_x$ and $P_y$ were varied from 220 nm to 320 nm; thus, the inter-disk gap was from 20 nm to 120 nm. The brightfield image of the arrays is shown in Figure 2B, while the unpolarized, *x*-polarized, and *y*-polarized darkfield images are shown in Figure 2C–E. The *x*-polarized and *y*-polarized images appear to be reflections of each other about the diagonal axis, while the unpolarized image is a sum of the *x*- and *y*-polarized images. The colors of the *x*-polarized darkfield image are arranged according to columns, which implies that the colors are affected more by the *x*-period than by the *y*-period.

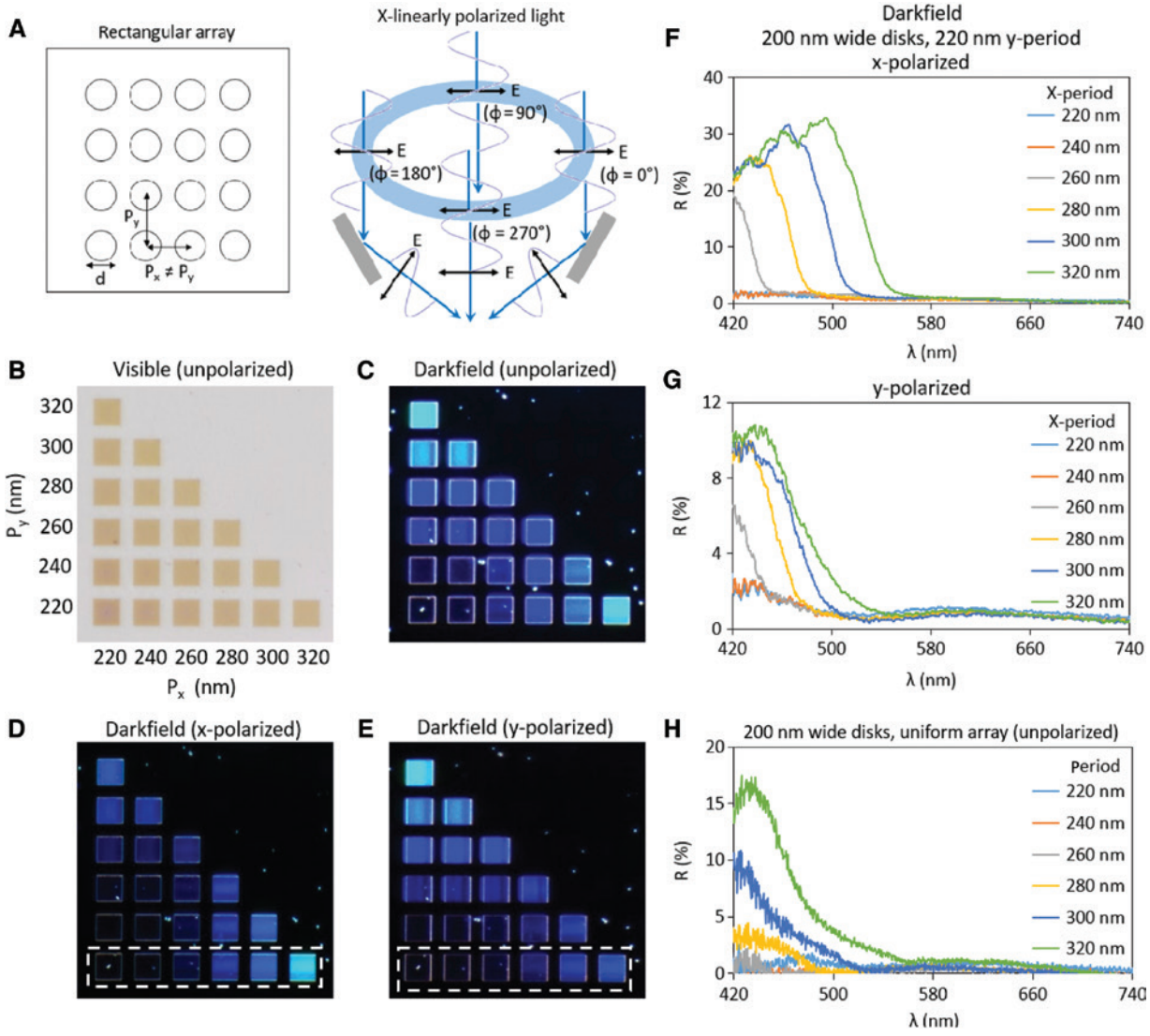


**Figure 2:** Polarization-dependent colors from rectangular arrays of single Al disks.
(A) Structure of rectangular disk array, where the *x*-period $P_x$ and *y*-period $P_y$ have different values. The electric fields for *x*-linearly polarized light are shown. (B) Unpolarized brightfield, (C) unpolarized, (D) *x*-polarized, and (E) *y*-polarized darkfield images of rectangular arrays of 200 nm wide Al disks. Both $P_x$ and $P_y$ are varied from 220 nm to 320 nm. The *x*-polarized and *y*-polarized images are nearly reflections of each other about the diagonal axis. (F) *x*-polarized and (G) *y*-polarized darkfield spectra for rectangular arrays of 200 nm wide disks, where $P_y$ is kept at 320 nm, while $P_x$ is from 220 nm to 320 nm. (H) Darkfield spectra for square arrays of single 200 nm wide disks under unpolarized incident light, where the period is from 220 nm to 320 nm.

We consider the bottom row of the arrays with a constant *y*-period of 220 nm, as indicated in Figure 2D and E. The *x*-period varies from 220 nm to 320 nm. Approximating the disk array as a 1D grating, for light incident from an azimuthal angle of 0° or 180°, the period of the grating is the *x*-period of the disk array (220 nm to 320 nm). Similarly, the period of the 1D grating encountered by light incident from an azimuthal angle of 90° or 270° is the *y*-period of the disk array (220 nm). From Table 1, when the incident light passes through an *x*-linear polarizer, the polarization states for 0°/180° and for 90°/270° are *p* and *s*, respectively, and since the diffraction efficiency is greater for *p*-polarization than for *s*-polarization, the intensity of diffracted light is stronger for the *x*-polarized configuration than for the *y*-polarized configuration. The spectra shown in Figure 2F and G support the colors in the darkfield images, as the spectra for *y*-polarization are compressed to the left and the amplitudes of the peaks are 30% of those for *x*-polarization. As diffraction occurs independent of the polarization of the incident light, the threshold wavelengths for the *x*-polarized and *y*-polarized spectra are similar. The reflectance spectra for 200 nm wide disks in square arrays are shown in Figure 2H for comparison and have narrower peaks than for the *x*-polarized spectra for the rectangular arrays. Thus, diffraction is more efficient when there is a smaller inter-disk gap in the axis perpendicular to the plane of the incident light, i.e. when the disk arrays resemble line gratings.

To find out the effect of plasmon resonances on the polarization dependence of the spectra, FDTD simulations were performed using a commercial program (FDTD Solutions) for a rectangular array of disks with 200 nm diameter, 320 nm *x*-period, and 220 nm *y*-period. The spectra from the simulations are shown in Figure 3A. Periodic boundary conditions were used, and the source light of 300–800 nm was delivered at a 63° angle to the sample surface from the right. The total reflected and diffracted light is collected by the field monitor placed above the sample. Note that this configuration does not represent experimental conditions as the monitor collects all light coming off the sample. When the source is incident at an angle, the reflectance for the disk array is highly polarization-dependent – the spectrum for *s*-polarized incident light is relatively flat, whereas the spectrum for *p*-polarized incident light has a sharp dip. The dip marks the wavelength at which the incident light is coupled to

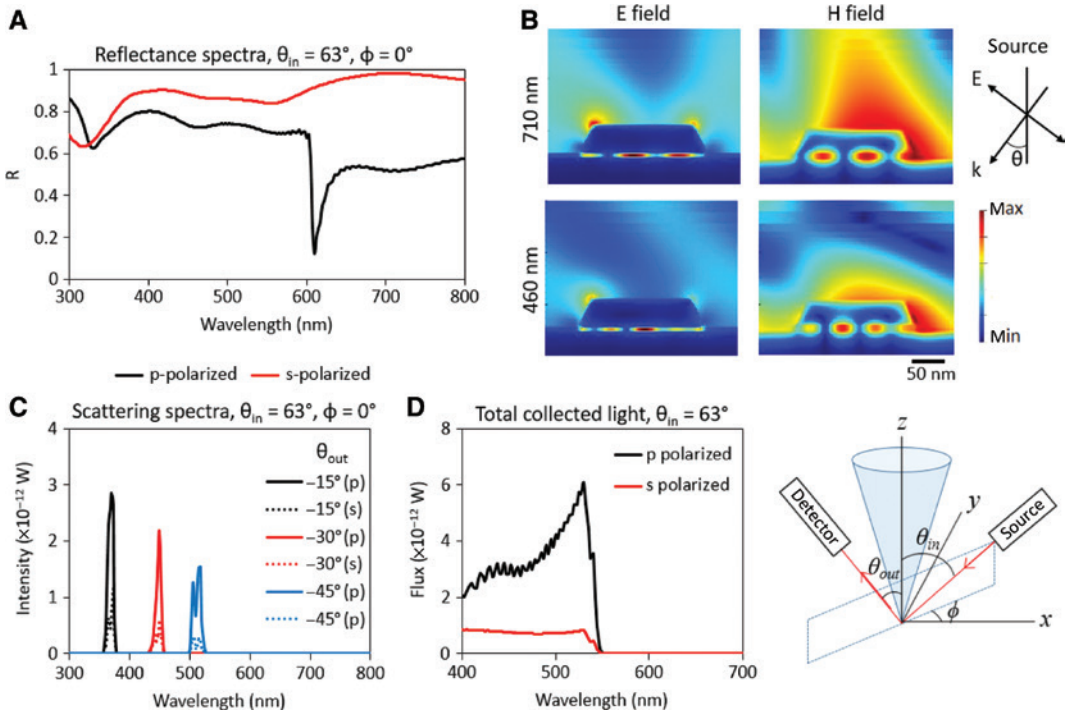


**Figure 3:** FDTD simulations of arrays of Al disks.
(A) Reflectance from a 63°-polar angle ($\theta$), 0°-azimuthal angle ($\phi$) plane wave source for an array of 200 nm wide disks with $P_x$ of 320 nm and $P_y$ of 220 nm. (B) Electric and magnetic fields for *p*-polarized illumination at 710 nm and 460 nm wavelengths. (C) Scattered field spectra for a rectangular array of 200 nm wide disks with $P_x$ of 320 nm and $P_y$ of 220 nm, under *p*- and *s*-polarized illumination from polar angle of 63° and azimuthal angle of 0°. Fields are collected at the same azimuthal angle and polar angles between 0° and 45°. (D) Total scattered light within a collection cone with half-angle of 53°, for *p*- and *s*-polarized illumination.

in-plane surface plasmons. This difference in the spectra also suggests that the diffraction efficiency for *p*-polarized light is higher than that for *s*-polarized light.

The electromagnetic fields from simulations are shown in Figure 3B. At the wavelength of 460 nm, the electric and magnetic fields correspond to the fourth-order resonance mode. The even resonance modes can only be stimulated when light is incident at an angle. The electric field is highest at the center of the base of the disk, with smaller regions of high field intensity at the extreme ends of the base of the disk. The magnetic field forms four anti-nodes at the edges of the base of each disk and is also high in the region between the disks. The smaller extent of the field maxima for this fourth-order mode causes the absorption to be weaker than for the fundamental mode. At a wavelength of 710 nm, the electric and magnetic fields of the disk array are markedly different and correspond to the grating mode. The electric field is highest in the gap below the disk and at the corners of the top surface of the disk. The magnetic field forms three maxima at the base of the disk, and the extreme right maximum lobe extends into the surrounding air. There is high absorption at the top circumference of the metal disk, so reflectance is low. The coupling of the incident light to the surface plasmon causes energy to propagate along the surface of the substrate, so little energy is reflected back in the vertical direction.

The FDTD simulated scattering spectra for a rectangular array of disks with a diameter of 200 nm, an *x*-period of 320 nm, and a *y*-period of 220 nm are also shown in Figure 3C. The incident plane wave has a polar angle $\theta_{in}$ of 63° and azimuthal angle $\phi$ of 0°, and far-field projection was carried out to calculate the diffracted light intensity at various points at a distance of 1 m from the sample. Diffracted light was collected in the same vertical plane (i.e. azimuthal angle $\phi$ fixed at 0°) at three different polar angles $\theta_{out}$ of –15°, –30°, and –45°. The negative signs mean that the light was diffracted backwards towards the source. The scattering peak observed at a polar angle of 0° occurs at a wavelength of 370 nm and redshifts to 450 nm and 510 nm when the polar angle increases, as predicted by the diffraction grating equation. In Figure 3D, the total scattered light flux that fits into a collection cone with a half-angle of 53° is calculated and plotted. Both the *p*-polarized and *s*-polarized spectra have a threshold wavelength of 550 nm, but the amplitude of the *p*-polarized spectrum is 2.5 to 10 times that for the *s*-polarized case, which shows that the diffraction efficiency is higher for the *p*-polarized light. The scattering spectra support the results shown in Figure 2F and G, as the shapes and peak ratios of the spectra are similar.

## 3.2 Disk clusters for increasing color gamut

To increase the range of hues obtained from the Al disk arrays, the layout of the disks was modified into clusters of disks, which causes the formation of an additional resonance mode by surface plasmon coupling. As shown in Figure 4A, the unit cell (basis) is a two-by-two cluster of disks with the same diameter and height, arranged in a square configuration. In other words, the array is a biperiodic two-dimensional grating, where the inter-disk gaps in the array have two fixed values. The smaller inter-disk gap is defined as $g_1$, while the larger inter-disk or inter-cluster gap is $g_2$. The scanning electron microscope (SEM) image taken of an array composed of 120 nm wide disks with $g_1 = 20$ nm and $g_2 = 120$ nm is shown in Figure 4B. The total period is 380 nm.

Darkfield and brightfield micrographs were taken of arrays of clusters of 80 nm wide, 100 nm wide, and 120 nm wide disks, as shown in Figure 4C–H. The inter-disk gap, $g_1$, is kept constant for each row, while the inter-cluster gap, $g_2$, is kept constant for each column. The darkfield colors are greatly expanded in hue compared to the colors for single-disk arrays. For the 80 nm wide disks, the darkfield colors are blue and cyan, indicating that the reflectance profiles for the various arrays are similar. For the 100 nm wide disks, the darkfield colors are redshifted to cyan and yellow, while for the 120 nm wide disks, the darkfield colors span yellow, pink, purple, and blue. This redshift occurs because the reflectance profiles become broader due to the increase in array periodicity and threshold wavelength. The brightfield colors for the 80 nm disks, 100 nm disks, and 120 nm disks are purple, dark cyan, and light green, respectively, and do not change with the inter-disk gaps. Thus, one is able to print arrays with a uniform brightfield color with varying darkfield colors and vice versa. The top left array for each set (marked with a red asterisk) has $g_1$ equal to $g_2$ and is identical to a single-disk array with an inter-disk gap equal to the disk diameter.

For the single-disk arrays, the darkfield colors for large disks are determined primarily by the period of the array, as the fundamental gap plasmon mode occurs at wavelengths larger than the threshold wavelength for collection by the darkfield objective (Figure S1). However, for the cluster arrays, the darkfield colors are dependent on both the period and the inter-disk gap. For instance, for 120 nm wide disks with a period of 480 nm, there are six possible values of $g_1 = 20$ nm, 40 nm, 60 nm, 80 nm, 100 nm, and 120 nm (marked with white asterisks). The colors start at yellow for $g_1 = 20$ nm and become dark purple for $g_1 = 80$ nm. The reflectance spectra for these arrays are shown in Figure 4I and have two peaks – one at

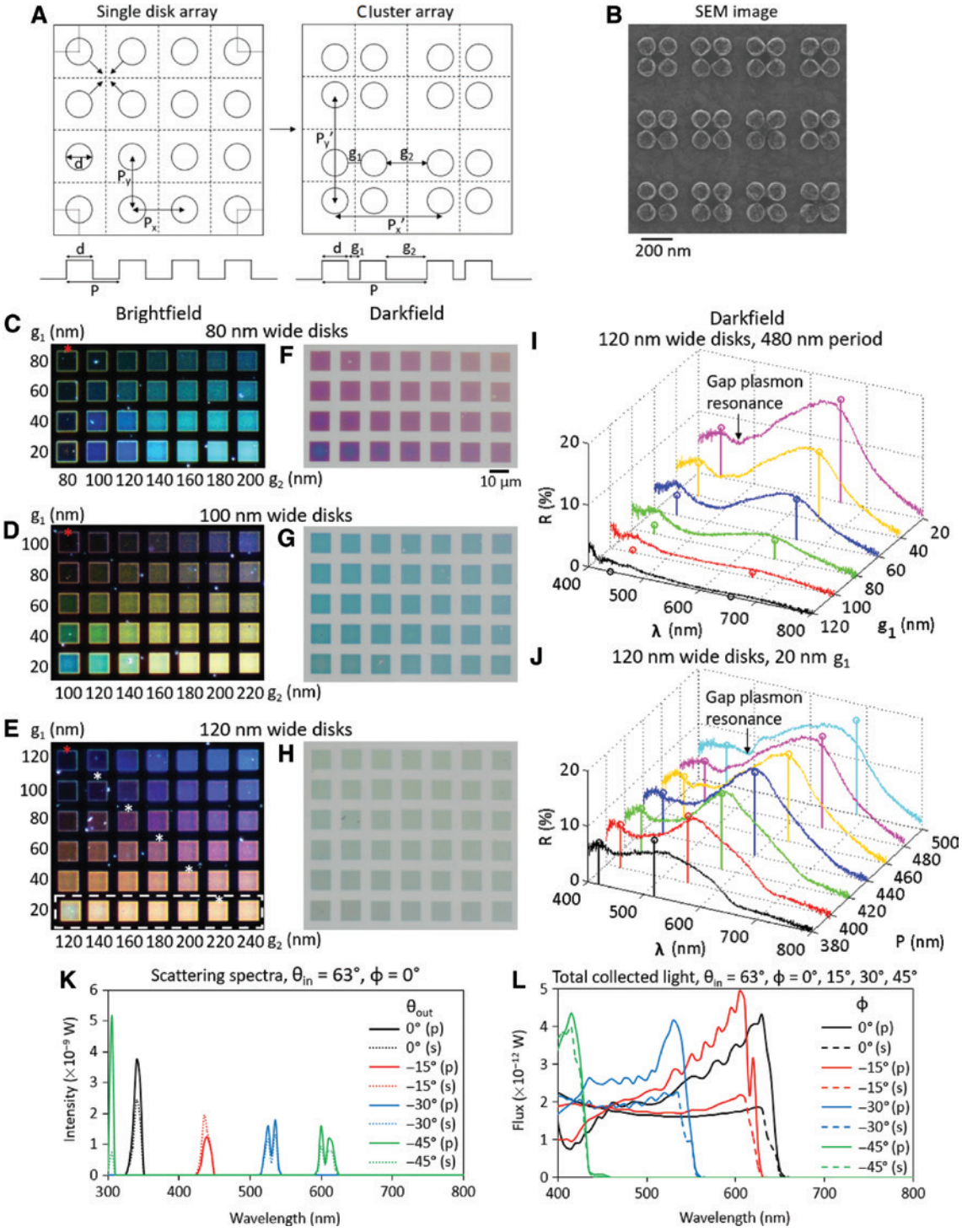


**Figure 4:** Darkfield colors from disk clusters.
(A) Schematic of array of single-disk and disk cluster arrays. The diameter $d$, period $P'$, inter-disk gap $g_1$, and inter-cluster gap $g_2$ are indicated. (B) SEM image of disk clusters with $d = 120$ nm, $g_1 = 20$ nm, and $g_2 = 120$ nm. Darkfield micrographs of (C) 80 nm wide disk clusters with $g_1$ from 20 nm to 80 nm and $g_2$ from 80 nm to 200 nm, (D) 100 nm wide disk clusters with $g_1$ from 20 nm to 100 nm and $g_2$ from 100 nm to 220 nm, and (E) 120 nm wide disk clusters with $g_1$ from 20 nm to 120 nm and $g_2$ from 120 nm to 240 nm. Brightfield micrographs of (F) 80 nm wide disk clusters, (G) 100 nm wide disk clusters and (H) 120 nm wide disk clusters. (I) Darkfield reflectance spectra for 120 nm wide disks and 480 nm period, with $g_1$ from 20 nm to 120 nm. (J) Darkfield spectra for 120 nm wide disks and $g_1$ of 20 nm, with a period from 380 nm to 500 nm. The normalized Fourier coefficients are also shown as open circles connected by vertical lines. (K) Scattered field spectra for array of 120 nm wide disk clusters with $g_1$ of 20 nm and a period of 380 nm, under $p$- and $s$-polarized illumination from polar angle of 63° and azimuthal angle of 0°. (L) Total collected light for disk cluster array under $p$- and $s$-polarized illumination from polar angle of 63° and azimuthal angles of 0°, 15°, 30°, and 45°.

a wavelength around 420 nm and another at a wavelength of 640 nm. The reflectance minimum between the peaks is caused by the gap plasmon mode around a wavelength of 480 nm (Figure S2), which also decreases the amplitude of the first reflectance peak. The wavelength position of the minimum shifts from 470 nm for $g_1 = 20$ nm, to 510 nm for $g_1 = 80$ nm, as the resonance energy of the plasmon has decreased. The main reflectance peak is attributable to first-order diffraction and is largest at 16% for $g_1 = 20$ nm, decreasing as $g_1$ becomes larger (1% for $g_1 = 100$ nm). The change in the relative amplitudes of the two peaks causes the perceived color to change from yellow for the smallest $g_1$ to pink and purple as $g_1$ increases.

We investigate the effects of an array with varying pitch but constant basis via the spectra in Figure 4J, which corresponds to the bottom row of the 120 nm wide disk arrays. The inter-disk gap $g_1$ is kept constant at 20 nm while the inter-cluster gap $g_2$ is between 120 nm and 240 nm. The spectral profile consists of a small peak around 420 nm and a larger, broader peak at a wavelength larger than 500 nm. The first peak is partially caused by the second-order and (1,1)th-order diffraction from the disk array, as the period is larger than the wavelength of incident light, which makes the grating vector shorter than the wave vector of light. The initial portion of the reflectance for wavelengths between 400 nm and 500 nm remains at an amplitude of 7%, as the contributions from the first-order and higher-order diffraction sum to a constant value. The inter-disk gap $g_1$ is fixed, so the plasmon resonance has the same energy and wavelength, and the absorbed energy by the resonance remains the same. Since the period increases from 380 nm to 500 nm, the threshold wavelength in the reflectance also increases from 680 nm to 810 nm. This broadening of the acceptance range of wavelengths also causes the amplitude of the second peak to increase, thus increasing the brightness of the colors.

In far-field diffraction, the Fraunhofer equation applies and the electric field amplitude of diffracted light is given by the Fourier transform of the diffracting aperture or object [30]. Here we assume that the first term of the Fourier series for an infinite 1D square grating gives a good approximation to the Fourier transform of the disk array. We calculate the Fourier amplitude for the $n$th order component of a square grating with width $d$, height $A$, and period $P$ to be

$$c_n^{\,2} = \left( \frac{2A}{\pi n} \sin\left( \frac{\pi n d}{P} \right) \right)^2, \tag{10}$$

whereas the amplitude for the $n$th order component of a biperiodic square grating with width $d$, height $A$, inter-disk gap $g_1$, and period $P$ is found to be

$$c_n^{\,2} = \left( \frac{2A}{\pi n} \sin\left( \frac{\pi n d}{P} \right) \cos\left( \pi n \left( \frac{g_1 + d}{P} \right) \right) \right)^2. \tag{11}$$

The normalized Fourier amplitudes are plotted as stems in Figure 4I and J and give good agreement to the trends for the spectra. The main peaks are due to the first-order diffraction. They increase with $g_1$ for the arrays of 120 nm wide disks with 440 nm period and increase with the period for the arrays of 120 nm wide disks with a fixed $g_1$ of 20 nm and periods between 380 nm and 440 nm. The Fourier amplitudes for the short-wavelength peaks in Figure 4J are algebraic sums of the squares of the amplitudes for the first-order and higher-order diffraction.

We verify the experimental reflectance spectra by plotting the simulated scattering spectra for an array of clusters of 120 nm wide disks with a period of 380 nm and $g_1$ of 20 nm in Figure 4K and L. In Figure 4K, light was collected at four different polar angles of 0°, 15°, 30°, and 45°, with the azimuthal angle fixed at 0°. The scattering peak observed at a polar angle of 0° occurs at a wavelength of 340 nm and shifts to longer wavelengths when the polar angle increases. For a polar angle of 45°, two peaks are observed, at 310 nm and 610 nm, as second-order diffraction also occurs for short wavelengths. The scattering amplitudes for the *p*-polarized and *s*-polarized incident light are similar, with the *p*-polarized amplitude being about 20% higher for polar angles of 30° and 45°.

In Figure 4L, the total collected light flux spectra for a 53°-half angle collection cone are shown for incident light with azimuthal angles $\phi$ of 0°, –15°, –30°, and –45°. The threshold wavelength decreases from 660 nm for $\phi$ of 0° to 440 nm for $\phi$ of –45°. As the incident light for sources with non-zero $\phi$ is no longer parallel to an axis of the disk array, two grating equations have to be satisfied, one for each axis of the disk array, which increases the polar angle of the output wave vector. For $\phi = 0°$, the *p*-polarized spectrum has a higher amplitude than the *s*-polarized spectrum for wavelengths between 450 nm and 660 nm and has a peak at 640 nm. This peak at 640 nm contributes to the main broad peak in Figure 4J. Also, the *p*-polarized spectrum has a dip at about 420 nm that is caused by the coupled plasmon resonance mode, which shows up as a small dip in the experimental spectrum in Figure 4J. When $\phi$ is –15° or –30°, the spectra are similar in profile to that for $\phi$ of 0°, as the *p*-polarized spectra exhibit a small peak close to the threshold wavelength and are larger than the *s*-polarized spectra for wavelengths larger than 470 nm and 420 nm, respectively.

## 3.3 Multi-level optical security tag

As an application of the optical characteristics of the Al gap plasmon resonators, one can design a multi-level print that serves an optical security tag. The print can encode an image only viewable under darkfield illumination while simultaneously displaying colors under brightfield illumination, so two images can be stored with low cross-talk. The darkfield image could be in the form of a barcode or other machine-readable identification code, which can be uniquely generated for a particular document, while the brightfield image could be a simple logo to aid the observer in locating the print on the document. The print thus serves as an authentication and anti-counterfeiting tool. The capability of encoding multiple images increases the security level of the tag, as the counterfeiter would need to duplicate all the images accurately. Alternatively, the print can also be made small enough to be indiscernible to the naked eye, to blend into a surrounding photograph or painting, but with sufficiently high resolution for viewing with a microscope.

Besides their diffractive properties, the Al resonators have also been shown to support infrared resonances when the disk diameter is above 120 nm, so they can absorb infrared light [12, 13]. Thus, an extra infrared image can also be encoded for a particular excitation wavelength (1.2 μm). The infrared image increases the difficulty of replicating the tag. Three pairs of disk arrays are necessary to encode the three images, which are namely a yellow-magenta brightfield visible color image, a blue-cyan-black darkfield visible color image, and a bright-dark infrared image. The parameters for the disks are shown in Table 2.

Finally, a fourth image can be encoded by utilizing the polarization-dependent two-dimensional grating property of rectangular arrays of disks. As shown previously, a disk array can have blue darkfield color under *x*-linear

**Table 2:** Physical parameters of disks used to make micro-tag.

| Number | Visible | IR (1.2 μm) | Darkfield | Diameter (nm) | Gap (nm) | Pitch (nm) |
|---|---|---|---|---|---|---|
| 1 | Yellow | Bright | Black | 60 | 40 | 100 |
| 2 | Yellow | Dark | Blue | 200 | 100 | 300 |
| 3 | Yellow | Dark | Cyan | 200 | 160 | 360 |
| 4 | Magenta | Bright | Black | 80 | 120 | 200 |
| 5 | Magenta | Dark | Blue | 230 | 70 | 300 |
| 6 | Magenta | Dark | Cyan | 230 | 130 | 360 |

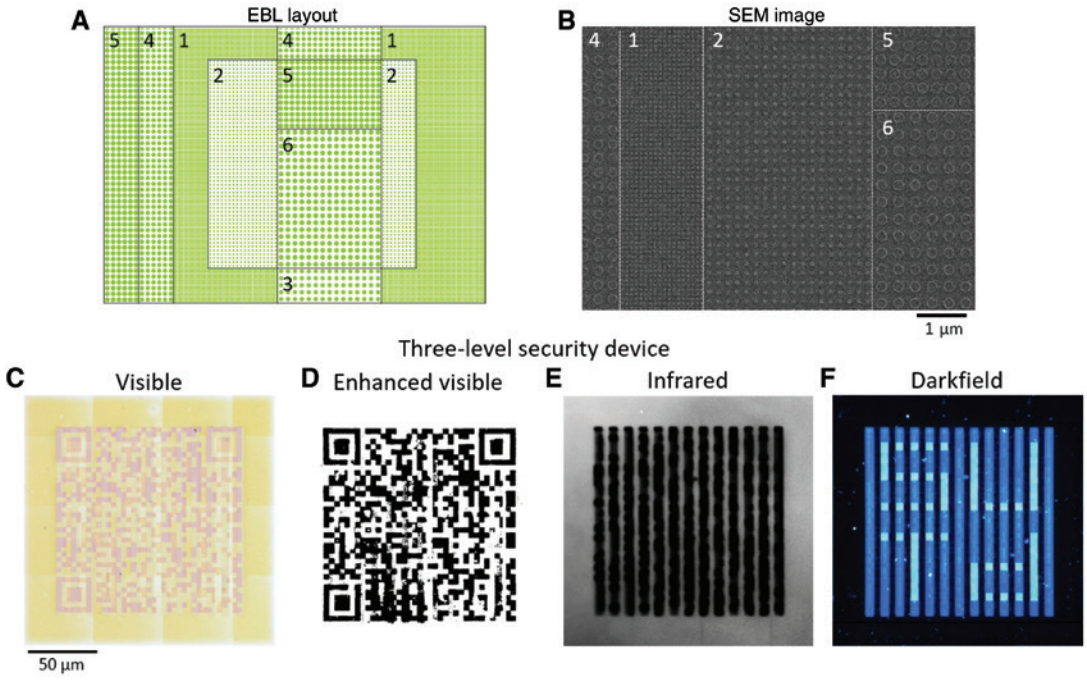


**Figure 5:** Multi-level optical micro-tag.
(A) Section of EBL layout of disks used for patterning. (B) SEM image of small region of fabricated tag. (C) Brightfield visible, (D) infrared, (E) *x*-polarized darkfield visible, and (F) *y*-polarized darkfield visible images of fabricated four-level security tag.

polarization and cyan darkfield color under *y*-linear polarization if the *x*-period and *y*-period are different. Thus, four more types of disk arrays were used to create two darkfield images, each visible under *x* or *y* linearly polarized light. The four additional arrays are (1) $d = 200$ nm, $P_x = 300$ nm, $P_y = 360$ nm; (2) $d = 200$ nm, $P_x = 360$ nm, $P_y = 300$ nm, (3) $d = 230$ nm, $P_x = 300$ nm, $P_y = 360$ nm, and (4) $d = 230$ nm, $P_x = 360$ nm, $P_y = 300$ nm.

We wrote a code in Matlab to read four image files and generate the layout file for performing electron-beam lithography, so that the appropriate disk diameter and pitch are defined for each pixel depending on the colors of the image file at the same pixel location. The pixel size is 1.8 μm, and the image size is 100 × 100 pixels. The security tag is then fabricated using EBL, electron beam evaporation, and lift-off. Sections of the EBL layout pattern and SEM image are shown in Figure 5A and B, where the different types of disk sizes and pitches are visible. The visible brightfield, infrared, and two visible darkfield images of the physical security tag are displayed in Figure 5C–F. The quality of the images is good, as the QR code, barcode, and letters “S”, “U”, “T”, “D”, “I”, “M”, “R”, and “E” can be clearly discerned.

## 4 Discussion

The darkfield reflectance spectra for arrays of aluminum disk MIM gap plasmon resonators have been measured and studied in terms of a two-dimensional diffraction grating. When the unit cell of the array is a single disk, the spectrum has the shape of a single peak with a side-lobe, giving rise to blue and cyan colors. However, when the unit cell is a two-by-two cluster of disks, the spectrum has two peaks due to absorption by the disks at their coupled plasmon resonance mode. This allows for the generation of a wide range of colors, including green, yellow, orange, pink, and purple, when the disk diameter and inter-disk gaps are adjusted.

To further investigate the physics of the darkfield response of the disk arrays, the periodicities of the arrays are modified so that their *x*- and *y*-periods are dissimilar. The arrays thus have two different reflectance spectra depending on the linear polarization of the input light. That the source of the polarization dependence in the spectra is the arrangement of the disks is advantageous for fabrication, as the geometry of the disk resonators is kept constant. The reflectance peak for the polarization corresponding to *p*-polarized incidence is 2 to 3 times larger than that corresponding to *s*-polarized incidence, as its diffraction efficiency is higher.

The broad range of darkfield colors and the feasibility of designing them via the disk diameter and inter-disk gaps make the Al gap plasmon structures promising for security printing and data storage. Previously, we had made dual-level security prints that encode information in the visible and infrared wavelength modes. With the results presented in this paper, one can now design four-level security prints that encode information in the visible wavelength, infrared wavelength, darkfield *x*-polarized, and darkfield *y*-polarized modes. Further extension is expected with the use of asymmetric geometries.

**Acknowledgments:** The authors would like to thank Jinfa Ho, Zhaogang Dong, Jonathan Trisno, Qifeng Ruan, and Hailong Liu for fruitful discussions and Senthilkumar Sakthivel and Sethu Narayan Tamilselvan for technical support and also acknowledge the following sources of funding: National Research Foundation (NRF) Competitive Research Programme (CRP) (15-2015-03, Funder Id: http://dx.doi.org/10.13039/501100001381) and SUTD Digital Manufacturing and Design (DManD) Centre (RGDM1830303).

**Disclosures:** The authors declare that there are no conflicts related to this work.

## References

[1] Choudhury SM, Wang D, Chaudhuri K, et al. Material platforms for optical metasurfaces. Nanophotonics 2018;7:959–87.
[2] Kristensen A, Yang JKW, Bozhevolnyi SI, et al. Plasmonic colour generation. Nat Rev Mater 2017;2:16088.
[3] Gu Y, Zhang L, Yang JKW, Yeo SP, Qiu CW. Color generation via subwavelength plasmonic nanostructures. Nanoscale 2015;7:6409–19.
[4] Kumar K, Duan H, Hegde RS, Koh SCW, Wei JN, Yang JKW. Printing colour at the optical diffraction limit. Nat Nanotechnol 2012;7:557–61.
[5] Roberts AS, Pors A, Albrektsen O, Bozhevolnyi SI. Subwavelength plasmonic color printing protected for ambient use. Nano Lett 2014;14:783–7.
[6] Clausen JS, Højlund-Nielsen E, Christiansen AB, et al. Plasmonic metasurfaces for coloration of plastic consumer products. Nano Lett 2014;14:4499–504.
[7] Goh XM, Zheng Y, Tan SJ, et al. Three-dimensional plasmonic stereoscopic prints in full colour. Nat Commun 2015;5:5361.
[8] Song M, Kudyshev ZA, Yu H, Boltasseva A, Shalaev VM, Kildishev AV. Achieving full-color generation with polarization-tunable perfect light absorption. Opt Mater Express 2019;9:779–87.
[9] Liu H, Xu J, Wang H, et al. Secure printing: tunable resonator-upconverted emission (TRUE) color printing and applications in optical security. Adv Mater 2019;31:1970106.

[10] Liu Y, Han F, Li F, et al. Inkjet-printed unclonable quantum dot fluorescent anti-counterfeiting labels with artificial intelligence authentication. Nat Commun 2019;10:2409.
[11] Hu D, Lu Y, Cao Y, et al. Laser-splashed three-dimensional plasmonic nanovolcanoes for steganography in angular anisotropy. ACS Nano 2018;12:9233–9.
[12] Ayas S, Topal AE, Cupallari A, Güner H, Bakan G, Dana A. Exploiting native $Al_2O_3$ for multispectral aluminum plasmonics. ACS Photonics 2014;1:1313–21.
[13] Ng RJH, Krishnan RV, Dong Z, et al. Micro-tags for art: covert visible and infrared images using gap plasmons in native aluminum oxide. Opt Mater Express 2019;9:788–801.
[14] Højlund-Nielsen E, Weirich J, Nørregaard J, Garnaes J, Mortensen NA, Kristensen A. Angle-independent structural colors of silicon. J Nanophotonics 2014;8:083988.
[15] Christiansen AB, Højlund-Nielsen E, Clausen JS, Caringal GP, Mortensen NA, Kristensen A. Imprinted and injection-molded nano-structured optical surfaces. Proc SPIE 2013;8818:881803.
[16] Murray WA, Barnes WL. Plasmonic materials. Adv Mater 2007;19:3771–82.
[17] Jiang L, Yin T, Dong Z, et al. Accurate modeling of dark-field scattering spectra of plasmonic nanostructures. ACS Nano 2015;9:10039–46.
[18] Mock JJ, Barbic M, Smith DR, Schultz DA, Schultz S. Shape effects in plasmon resonance of individual colloidal silver nanoparticles. J Chem Phys 2002;116:6755–9.
[19] Knight MW, Fan J, Capasso F, Halas NJ. Influence of excitation and collection geometry on the dark field spectra of individual plasmonic nanostructures. Opt Express 2010;18:2579–87.
[20] Olson J, Manjavacas A, Liu L, et al. Vivid, full-color aluminum plasmonic pixels. Proc Natl Acad Sci USA 2014;111:14348–53.
[21] Olson J, Manjavacas A, Basu T, et al. High chromaticity aluminum plasmonic pixels for active liquid crystal displays. ACS Nano 2016;10:1108–17.
[22] Rezaei SD, Ho J, Ng RJH, Ramakrishna S, Yang JKW. On the correlation of absorption cross-section with plasmonic color generation. Opt Express 2017;25:27652–64.
[23] Wang D, Yang A, Hryn AJ, Schatz GC, Odom TW. Superlattice plasmons in hierarchical Au nanoparticle arrays. ACS Photonics 2015;2:1789–94.
[24] Kwadrin A, Koenderink AF. Diffractive stacks of metamaterial lattices with a complex unit cell: self-consistent long-range bianisotropic interactions in experiment and theory. Phys Rev B 2014;89:045120.
[25] Baur S, Sanders S, Manjavacas A. Hybridization of lattice resonances. ACS Nano 2018;12:1618–29.
[26] Mertens J, Eiden AL, Sigle DO, et al. Controlling subnanometer gaps in plasmonic dimers using graphene. Nano Lett 2013;13:5033–8.
[27] Zhang Y, Liu QK, Mundoor H, Yuan Y, Smalyukh II. Metal nanoparticle dispersion, alignment, and assembly in nematic liquid crystals for applications in switchable plasmonic color filters and e-polarizers. ACS Nano 2015;9:3097–108.
[28] Heydari E, Sperling JR, Neale SL, Clark AW. Plasmonic color filters as dual-state nanopixels for high-density microimage encoding. Adv Funct Mater 2017;27:1701866.
[29] Yun H, Lee SY, Hong K, Yeom J, Lee B. Plasmonic cavity-apertures as dynamic pixels for the simultaneous control of colour and intensity. Nat Commun 2015;6:7133.
[30] Born M, Wolf E. Principles of optics, 7th ed. Cambridge, UK, Cambridge University Press, 1999.

**Supplementary Material:** The online version of this article offers supplementary material (https://doi.org/10.1515/nanoph-2019-0414).

# Bionote

**Ray Jia Hong Ng**
Singapore University of Technology and Design, Engineering Product Development Pillar, Singapore 487372, Singapore.
https://orcid.org/0000-0003-2540-2922

Ray Jia Hong Ng is a PhD student at the Singapore University of Technology and Design. He received his BA degree in Physics from the University of Chicago in 2010 and his MS degree in Applied Physics from Harvard University in 2013. He is the author of more than 10 journal papers. His current research interests include nanoplasmonics, plasmonic color printing, and optical security devices.